

# Exploring the Stability and Residual RVS Effects in SNPP VIIRS SDR Reflectance Products Using Deep Convective Clouds

Qiaozhen Mu,<sup>a</sup> Xiaoxiong Xiong,<sup>b</sup> Tiejun Chang,<sup>a</sup> Aisheng Wu<sup>a</sup>

<sup>a</sup>Science Systems and Applications, Inc, 10210 Greenbelt Road, Lanham, MD 20706

<sup>b</sup>Sciences and Exploration Directorate, NASA/GSFC, Greenbelt, MD 20771

**Abstract:** The reflective solar bands (RSB) of the Visible and Infrared Imaging Radiometer Suite (VIIRS) on Suomi National Polar-orbiting Partnership (SNPP) satellite are calibrated using solar diffuser and lunar observations. To evaluate the performance of the VIIRS RSB calibration, the deep convective clouds (DCC) are utilized as invariant targets to assess the stability of NASA's VIIRS sensor data record (SDR) reflectance product for 10 moderate resolution bands (M-bands, M1–M5 and M7–M11) and three imagery resolution bands (I-bands, I1–I3). All the frames along each scan are divided into six aggregation zones for the scan angle. An empirical Bidirectional Reflectance Distribution Function (BRDF) correction is performed to SDR reflectances over DCC to reduce the scattering anisotropy in view and solar angles. The BRDF-corrected reflectances are used to assess the stability and to explore the residual RVS effects for select bands. Results of this study show that after more than six years of on-orbit operation, use of the prelaunch-based RVS still meets the radiometric requirement for the VIIRS RSB. Examination of the small but noticeable RVS residuals indicates they occur in a few shortest wavelength bands based on a time-dependent quadratic fit of the reflectance trends obtained at all scan angle zones. As mission continues, continuing monitoring of on-orbit RVS stability and its effects on VIIRS SDR reflectance products is necessary with the DCC technique in the future VIIRS calibrations to assure the quality of the RSB SDR products.

**Key Words:** reflective solar bands (RSB), SNPP VIIRS, stability assessment, response versus scan angle (RVS), angle of incidence (AOI), Bidirectional Reflectance Distribution Function (BRDF)

\*First Author, E-mail: [qiaozhen.mu@ssaihq.com](mailto:qiaozhen.mu@ssaihq.com)

## 1 Introduction

The Joint Polar Satellite System (JPSS) was established in year 2010 as a result of a restructuring the National Polar-orbiting Environmental Satellite System (NPOESS), to provide continuity of critical observations for NOAA's polar-orbiting operational environmental satellite system (POES)<sup>1</sup>. The Suomi National Polar-orbiting Partnership (SNPP) satellite serves as a gap filler between the POES satellites of JPSS due to schedule delays<sup>2</sup>. The Visible and Infrared Imaging Radiometer Suite (VIIRS) is one of the five key instruments onboard the SNPP satellite launched on October 28, 2011. VIIRS was developed based on a long heritage of legacy operational and research instruments, which dates back as early as the late 1970s. Key heritage instruments

include Advanced Very High Resolution Radiometer (AVHRR) onboard NOAA <sup>3</sup>, Operational Linescan System (OLS) onboard Defense Meteorological Satellite Program (DMSP) <sup>4</sup>, and Moderate Resolution Imaging Spectroradiometer (MODIS) on Terra and Aqua <sup>5</sup>. VIIRS provides calibrated Top-Of-Atmosphere (TOA) radiance, reflectance and brightness temperature Sensor Data Records (SDRs) for weather and climate applications similar to its predecessors.

SNPP is in a sun-synchronous orbit with an altitude of ~828 km, an equatorial crossing of 13:30 and swath width of about 3000 km <sup>2, 6</sup>. SNPP-VIIRS has 14 Reflective Solar Bands (RSB), seven Thermal Emissive Bands (TEB) and a panchromatic Day Night Band (DNB), with a spectral range from 0.41  $\mu\text{m}$  to 12.013  $\mu\text{m}$ . VIIRS TEB are calibrated using an on-board blackbody (BB). VIIRS RSB are calibrated with a solar diffuser (SD) and lunar observations <sup>2, 7-9</sup>. The 14 VIIRS RSB include 11 moderate resolution bands (M-bands, M1-M11) and three imagery resolution bands (I-bands, I1-I3). The seven VIIRS TEB include five M-bands (M12-M16) and two I-bands (I4-I5). In this study, the performance of the VIIRS RSB calibration is assessed using NASA's Land Science Investigator-led Processing System (LSIPS) V5000 C1 VIIRS SDR products (<https://ladsweb.modaps.eosdis.nasa.gov/>), hereafter called LSIPS VIIRS SDR products. The LSIPS VIIRS SDR products are calibrated using the look-up-tables (LUTs) delivered by NASA VIIRS Characterization Support Team <sup>10-12</sup>. Fig. 1a shows the schematic diagram of onboard calibrations for VIIRS. An onboard SD stability monitor (SDSM) is designed to measure the change in the Bidirectional Reflectance Distribution Function (BRDF) of the SD at the SDSM SD view direction <sup>13-15</sup>. VIIRS RSB spectral wavelengths range from 0.41  $\mu\text{m}$  to 2.25  $\mu\text{m}$ . SDSM has eight detectors with wavelength ranging between 0.412  $\mu\text{m}$  and 0.935  $\mu\text{m}$ . Table 1 shows the center wavelengths (CW) of the eight SDSM detectors and their corresponding VIIRS RSB. The center wavelengths of the shortwave Infrared bands (SWIR)

M8-M11 are beyond the range of the SDSM detector wavelengths and the SD degradation for the SWIR bands cannot be tracked. Lei and Xiong<sup>15</sup> developed empirical models to estimate the SD degradation (H-factor) at the SWIR band wavelengths. Due to the dependency of H-factor on view angles relative to both the sun and SD, SD H-factor and VIIRS instrumental calibration coefficients (F-factor) are derived by combining the SD-based and lunar-based observations<sup>12</sup>. The raw digital numbers (DNs) from earth view (EV) observations in VIIRS raw data record (RDR) are converted into various LSIPS VIIRS SDR radiance products using F-factor LUTs and response versus scan angle (RVS) measured prelaunch<sup>16</sup>. These VIIRS SDR products include calibrated top of atmosphere (TOA) radiance, TOA reflectance, and TOA brightness temperature. In the VIIRS calibration algorithm, DNs from the onboard calibrator blackbody (BB), space view (SV), and SD view are first adjusted for background signal levels, and then are utilized to update calibration coefficients for VIIRS RSB.

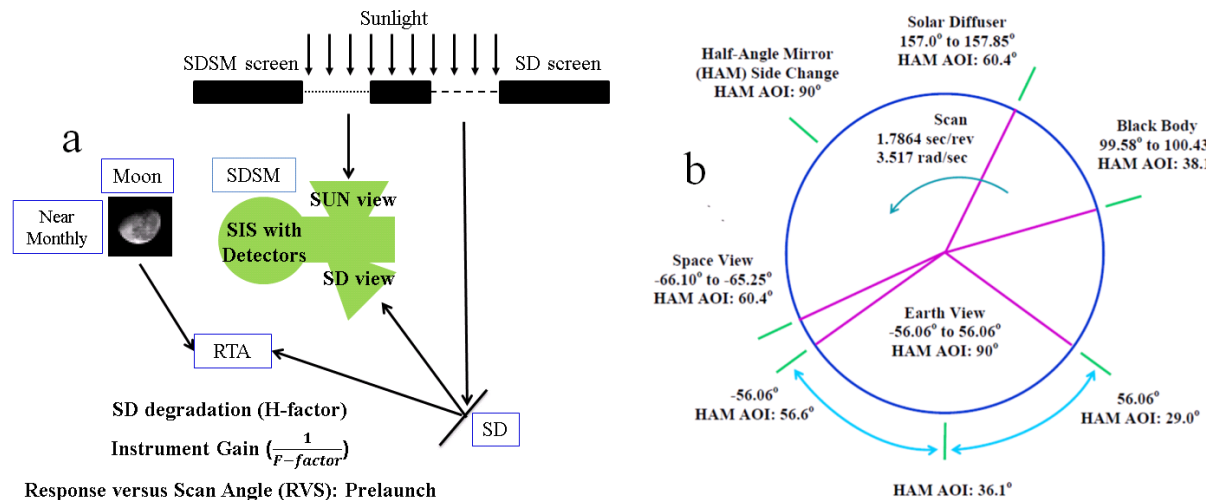


**Fig. 1** (a) Schematic diagram of VIIRS onboard calibrations for VIIRS reflective solar bands (RSB); (b) scan angles of VIIRS view sectors and their corresponding Angles of Incidence (AOIs) on the Half Angle Mirror (HAM). SD: Solar Diffuser; SDSM: SD stability monitor; SIS: Spherical Integrating Source; RTA: Rotating Telescope Assembly.

**Table 1** Center wavelengths (CW) of the eight Solar Diffuser Stability Monitor (SDSM) detectors in  $\mu\text{m}$ , and CW and bandwidths (BW) in nm and locations of the Focal Plane Assembly (FPA) of VIIRS RSB. Selected RSB in this study: 10 moderate resolution bands (M-bands, M1-M5 and M7-M11), and three imagery resolution bands (I-bands, I1-I3). M6 saturates over deep convective clouds (DCC).

SDSM		VIIRS RSB			FPA
Detector	CW ( $\mu\text{m}$ )	Band	CW ( $\mu\text{m}$ )	BW (nm)	
D1	0.412	M1	0.412	20	VIS/NIR
D2	0.450	M2	0.445	18	
D3	0.488	M3	0.488	20	
D4	0.555	M4	0.555	20	
		I1	0.640	80	
D5	0.672	M5	0.672	20	
D6	0.746	M6	0.746	15	
D7	0.865	M7, I2	0.865	39	
D8	0.935				
		M8	1.240	20	
		M9	1.378	15	SWIR
		M10, I3	1.610	60	
		M11	2.250	50	

VIIRS views the SV, EV, BB, and SD via a four-mirror Rotating Telescope Assembly (RTA) cross-track scanner combined with a Half Angle Mirror (HAM) that directs light exiting from the RTA into the aft-optics<sup>6</sup>. Fig. 1b shows the scan angle as well as the angle of incidence (AOI) for each view<sup>16</sup>. The RTA and aft-optics have fixed AOIs for each band and detector but the HAM AOI is dependent on the scan angle, with a variation of 29.0° to 56.6° over the full EV scan angle (Fig. 1b). The RVS effects exist due to the wide AOI range of the HAM for the EV scan. The RVS was measured prelaunch but may change on-orbit due to the degradation of the HAM as previously observed Aqua and Terra MODIS scan mirror<sup>17</sup>. VIIRS HAM degrades much slower than the MODIS instruments at the short wavelength VIS bands<sup>18</sup> because VIIRS HAM is inside the instrument and the scan mirrors on MODIS directly face the Earth's surfaces<sup>18</sup>. In the current VIIRS calibrations, only the instrumental degradation F-factor is considered time-dependent; the prelaunch measured RVS is used as constant over time, which might not be

adequate. To monitor the performance and effectiveness of the VIIRS RSB on-orbit calibrations, pseudo-invariant targets such as deep convective clouds (DCC)<sup>19-21</sup>, deserts and Dome-C<sup>22-25</sup> are used to track the long-term stability and residual RVS effects in VIIRS SDR products. Previous studies using the DCC technique (DCCT) have been carried out to assess the stability of the VIIRS SDR products for RSB and sensitivity of VIIRS DCCT to different DCCT parameters<sup>19-23</sup>. In this study, DCCT is utilized to assess the performance of the current VIIRS calibrations by using the reflectance in LSIPS VIIRS SDR product for 10 M-bands (M1–M5 and M7–M11) and three I-bands (I1–I3). Band M6 saturates over DCC and is not considered in this work. The residual RVS effects in the SDR product will also be evaluated by comparing reflectances from different AOIs. The long-term drifts and the residual RVS effects in SDR reflectance over DCC for VIIRS RSB will be monitored to support future improvements in the VIIRS SDR products. Section 2 briefly describes the methodology of DCC identification, DCC reflectance derivation, and an empirical BRDF correction. Section 3 discusses the stability assessment results, the residual RVS effect exploration results, and the comparison results between DCC and deserts. Section 4 summarizes major results from this study. This study is an improvement to the work presented by Mu et al.<sup>26</sup>.

## **2 Methodology**

This section describes the data source and pre-processing, DCC identification criteria and process, and the BRDF method to correct reflectance over DCC samples.

### *2.1 Background and Data Preprocessing*

LSIPS VIIRS SDR for RSB are generated by calibrating VIIRS RDR using calibration coefficients F-factor derived from the onboard SD and lunar observations<sup>12</sup> and pre-launch RVS

<sup>16</sup>. The VIIRS SDR products are further used by downstream users to generate science data sets. VIIRS SDR products for RSB provide data for 11 M-bands (M1-M11) and three I-bands (I1-I3). The purpose of this study is to assess the long-term stability of SDR reflectance data and to explore the residual RVS effects in LSIPS VIIRS SDR reflectance product using DCCT. In order to downsize the large volume of daily global data, earth view data from LSIPS V5000 C1 VIIRS SDR products over the eastern Indian and western Pacific Oceans (30°S-30°N and 95°E-175°E) are utilized to identify the DCC samples for stability analyses and residual RVS effect detection. The reflectance data in LSIPS VIIRS SDR products are used in this study. M15 (10.26–11.26  $\mu\text{m}$ ) provides brightness temperature (BT) measurements required for DCC pixel identification. I5 (11.45–1.9  $\mu\text{m}$ ) can also provide BT. The CW and BW of M15 are 10.763  $\mu\text{m}$  and 1.0  $\mu\text{m}$ , 11.45  $\mu\text{m}$  and 1.9  $\mu\text{m}$  for I5. In this study, we aggregate the 375-m I-band reflectance data into 750-m data, which has the same spatial resolution as M-bands. The spectral width of 1.9  $\mu\text{m}$  for I5 is much wider than 1.0  $\mu\text{m}$  for M15. The spectral band design noise specification is 0.07 K for M15 BT and 1.5 K for I5 BT <sup>2, 10</sup>. Chang et al. <sup>20</sup> find that the DCC identification using M15 BT has a tighter constraint than using I5 BT. To minimize the misidentification of DCC samples caused by the difference in the BT between M15 and I5, the M15 BT is used for identification of DCC for both the M-bands and the aggregated I-bands. The geo-location data for M-bands is also used for the aggregated I-bands. The SDR data covering the time period from February 2012 to June 2018 are used to assess the long-term calibration performance and residual RVS effects of VIIRS RSB.

In each LSIPS VIIRS SDR granule, the HAM AOIs range from 29.0° to 56.6° with the full EV view angles between -56° and 56°, and frame numbers range between 1 and 3200. All the frames along each scan are divided into the six aggregation zones (Z1-Z6) <sup>27</sup> according to the

frame numbers as listed in Table 2 for the M-bands and aggregated I-bands. The relationship between frame numbers, scan angles and AOIs are described by Baker<sup>6, 27</sup>. The AOI of one frame along track is calculated as in Equation 1.

$$\theta = -56.063^\circ + 56.063^\circ * 2.0 * \frac{f - 1}{3199}$$

$$AOI = \cos^{-1}\{\cos(28.6^\circ) * \cos[0.5 * (\theta - 46.0^\circ)]\} \quad (1)$$

where  $f$  is frame number. Table 2 lists the ranges of frame numbers, scan angles, zenith angles, and AOIs in Z1-Z6. Reflectance data over DCC samples are utilized to assess the long-term trending of SDR products and the residual RVS effects in the six zones. The pixels impacted by the bow-tie effects<sup>27</sup> are excluded in the DCC identification process. The latitude is limited between (30°S–30°N) to identify DCC in the tropical region.

**Table 2** Aggregation frame zones (Z1-Z6) for M-bands and aggregated I-bands at 750-m spatial resolution with 3200 frames along scan, and the frame number range, start scan angle, end scan angle, start zenith angle, end zenith angle, start AOI, and end AOI for each aggregation zone.

Aggregation Zone	Z1	Z2	Z3	Z4	Z5	Z6
Frame Number	1–640	641–1008	1009–1600	1601–2192	2193–2560	2561–3200
Start Scan Angle	-56°	-43°	-32°	0°	32°	43°
End Scan Angle	-43°	-32°	0°	32°	43°	56°
Start Zenith Angle	69.4	52.6	36.7	0	36.7	52.6
End Zenith Angle	52.6	36.7	0	36.7	52.6	69.4
Start AOI	47.61°	42.85°	36.09°	31.05°	29.21°	29.00°
End AOI	56.48°	47.59°	42.84°	36.08°	31.04°	29.20°

The Earth's surface scatters radiation in an anisotropic manner, especially at the shorter wavelengths. The BRDF specifies the behavior of surface scattering as a function of illumination and view angles at a particular wavelength<sup>28</sup>. In this study, an empirical BRDF correction based on the reflectance over 02/2012-01/2017 for each M-band is performed to adjust the view and illumination angle effects on the SDR reflectance product. For the I-bands, the BRDF correction

is performed using the coefficients derived for their corresponding M-bands with close center wavelengths. More details can be found in sub-section 2.2.2.

## 2.2 Application of DCCT

### 2.2.1. Identification of DCC

DCC are clouds undergoing intense convection. They are the coldest natural earth targets in the tropics and can be easily identified using a BT threshold from an infrared (IR) band <sup>29</sup>. The advantage of the DCCT over clear-sky surface based sites is that DCC are at the tropopause level, where the atmospheric effects such as absorption are significantly reduced with the exception of stratospheric aerosols. They are bright earth targets illuminated via a greater sun elevation angle in the tropics as compared to the oblique sun angles at Dome-C and therefore have a greater signal to noise ratio (SNR) <sup>30</sup>. DCC can be treated as solar diffusers, which have predictable and near Lambertian albedos <sup>29</sup>.

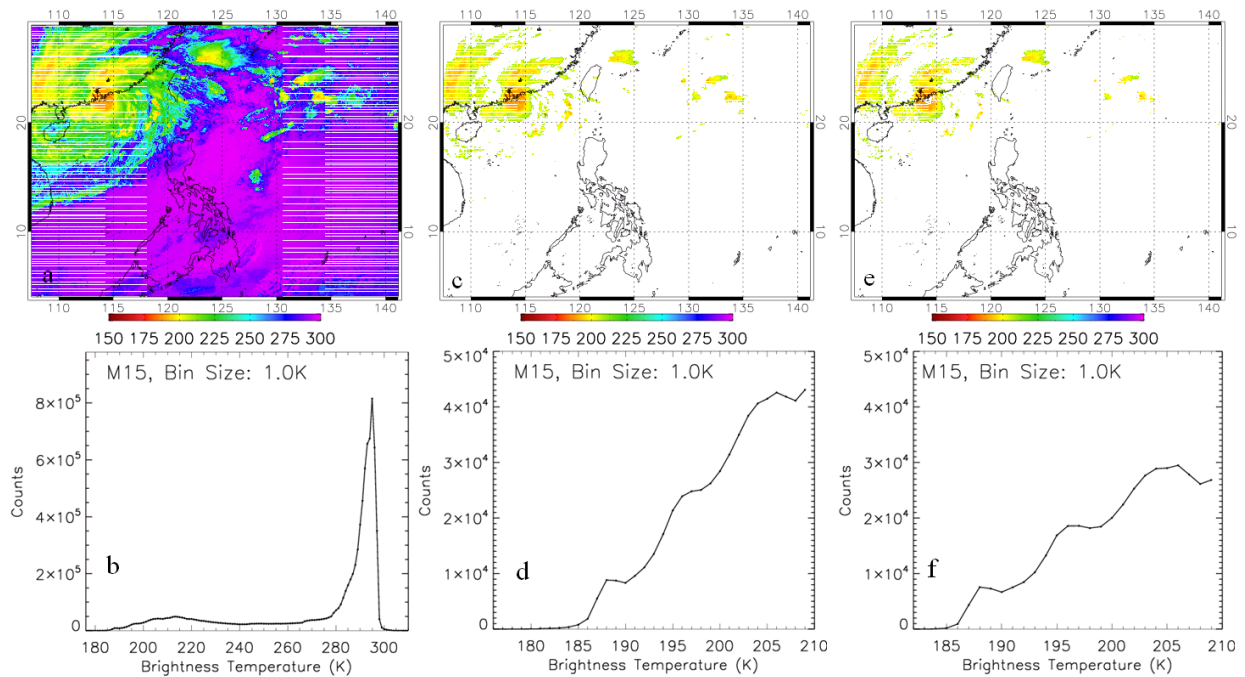




**Fig. 2** Spatial patterns and their corresponding histograms of 11- $\mu$ m moderate resolution band M15 brightness temperature (BT11) for LSIPS VIIRS V5000 SDR granule 2014305.0500 on 11/01/2014 using: all valid frames (a, b); potential deep convective cloud (DCC) frames (c, d) and DCC frames (e, f) with BT11 less than 210 K before and after the spatial uniformity test, respectively. Gray color in the spatial maps represents pixels with filled value.

The first step of DCC identification process is to use the threshold value of 210 K for VIIRS 11- $\mu$ m M15 brightness temperature (BT11) to identify the potential DCC<sup>31</sup>. The DCC samples with reflectance impacted by saturation or bow-tie effects (Baker, 2011) are excluded from further analyses. The latitude is limited between (30°S–30°N) to identify DCC in the tropical region. In the second step, to avoid pixels that contain DCC cloud edges and anvils, a uniformity test is performed over a 3 by 3 pixel block surrounding the centered DCC pixel (750-m spatial resolution). Doelling et al.<sup>29, 32</sup> recommended using the reflectance at 0.65  $\mu$ m and BT at 11  $\mu$ m to do the uniformity test for MODIS. The center DCC pixel is rejected if the spatial standard deviation (STD) of BT11 from M15 over the 3 by 3 pixel block is greater than 1 K, or if the spatial STD of reflectance from M5 at  $\sim$ 0.67  $\mu$ m for M-bands, from I1 at the  $\sim$ 0.64  $\mu$ m for I-bands, is greater than 3% of the average reflectance over the 3 by 3 block<sup>29, 32</sup>. Fig. 2 shows spatial patterns and histograms of VIIRS pixel-level M15 BT11 for one LSIPS VIIRS SDR granule 2014305.0500 on 11/01/2014 using all frames with valid BT11 values (Fig. 2a, b), potential DCC frames (Fig. 2c, d) and DCC frames (Fig. 2e, f) with BT11 less than 210 K before and after the spatial uniformity test, respectively. The criterion of BT11 < 210 K identifies a small portion of valid pixels as potential DCC pixels. The uniformity test screens out the misclassified DCC samples and reduces the frequency of identified DCC in the first step. The histograms of BT11 over the DCC pixels change before (Fig. 2e) and after (Fig. 2f) the uniformity test accordingly. The uniformity test is necessary to choose the high-quality DCC

pixels. The final step of the DCC identification is to choose the actual DCC pixels using the criterion of BT11 smaller than the threshold value of 205 K.

### 2.2.2. BRDF Correction

The stability of the SDR reflectance products is checked based on the mean reflectance or the mode reflectance obtained from the probability distribution function (PDF) of reflectances over DCC collected over a certain time period <sup>32</sup>. Doelling et al. <sup>32</sup> found that the mode statistic is superior to the mean statistic when there are sufficient DCC samples and the PDFs are smooth. In this study, the mode reflectances are used to assess the performance of RSB calibrations. Monthly time interval is used as the DCC sample collection time period for each mode reflectance data. Fig. 3a and Fig. 3c show the PDFs of monthly reflectances over DCC in each May over study time period 02/2012-06/2018 for M5 (center wavelength 0.672  $\mu\text{m}$ ) and I1 (center wavelength 0.64  $\mu\text{m}$ ) in Z3 around nadir where the bow-tie effect is small <sup>27</sup> and the zenith angles are less than 40° (Table 2).

To minimize the potential impact of the BRDF effects on the reflectances at different wavelengths over the DCC, an empirical BRDF correction is performed to correct the reflectance data. First, solar zenith angle (SZA), view zenith angle (VZA) and relative azimuth angle (rela-AZ) are evenly divided into 18 x 18 x 18 bins, with a resolution of 5° x 5° x 10° for each bin. The DCC samples over the 5-year time period 02/2012-01/2017 are distributed into these angular bins according to their angles. Due to the insufficient DCC samples for some bins, the mean reflectance instead of the mode during the five years for each M-band is calculated to derive the BRDF correction coefficient for each angular bin. Secondly, at each DCC pixel, the equivalent BRDF-corrected reflectance is calculated as the ratio of the reflectance to the average BRDF coefficients over all the neighboring bins with maximum seven bins containing valid BRDF

coefficients for each M-band. The seven possible bins for correction include the one close to the DCC pixel, two neighboring bins along the SZA direction, two along the VZA direction, and two along the rela-AZ direction. For three I-bands I1-I3, the BRDF coefficients are from M5, M7 and M10, which have the closest spectrum to their corresponding I-bands, respectively. Fig. 3b and Fig. 3d show the monthly PDFs of BRDF-corrected reflectance in each May for M5 and I1 corresponding to PDFs of reflectance in Fig. 3a and Fig. 3c for Z3. The PDFs are smoother after the BRDF correction. The temporal STDs of monthly mode reflectances over DCC are reduced from 1.01% to 0.92% for M5, and from 1.12% to 0.92% for I1 in Z3. The trend is 0.47% for M5 and reduces from 0.65% to 0.52% for I1. More results for all the study RSB are discussed in Section 3.

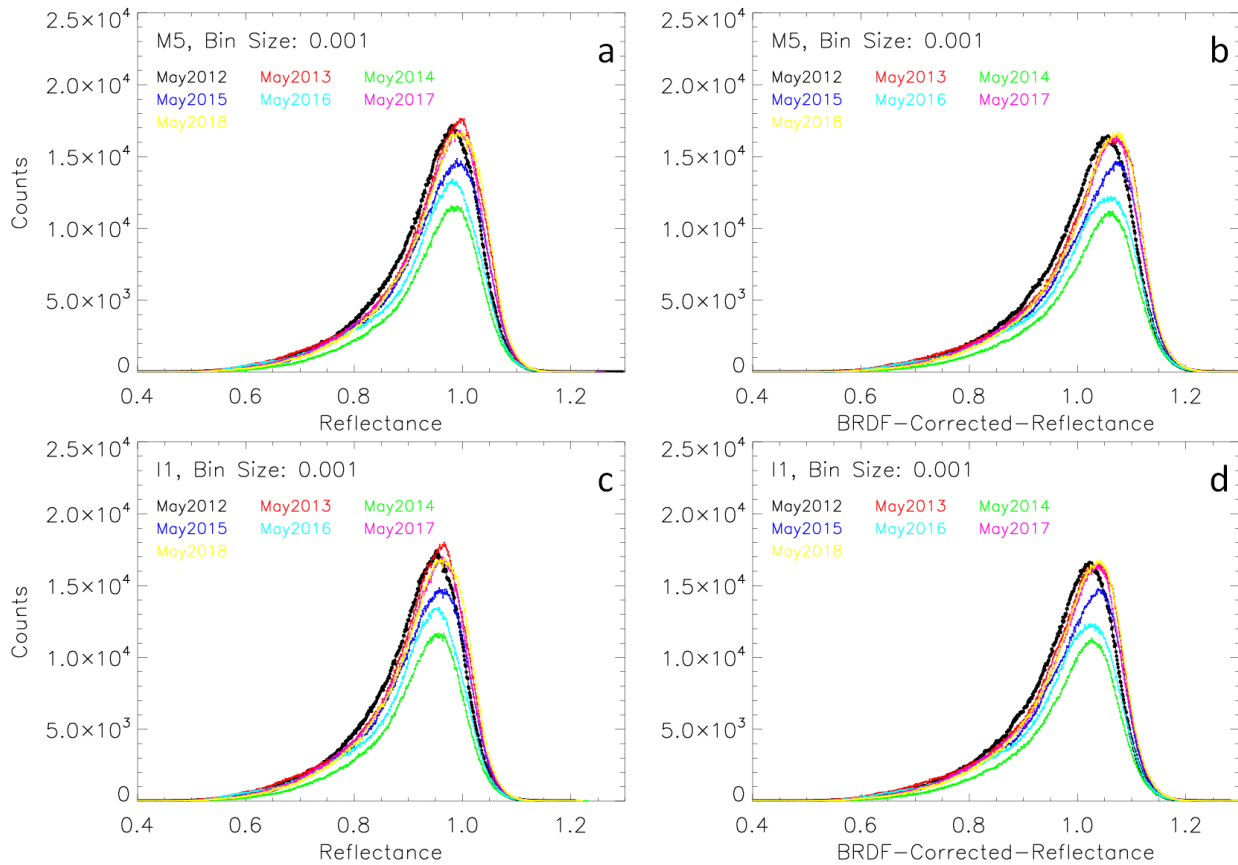


**Fig. 3.** Monthly probability distribution functions (PDF) of reflectance before (Left Panel) and after the BRDF correction (Right Panel) over DCC for M5 (a, b) and I1 (c, d) in each May over 02/201-06/2018 in zone 3.

## 3 Results and Discussions

### 3.1 BRDF Correction

#### 3.1.1 Evaluation of BRDF Correction

To evaluate the performance of the empirical BRDF correction method, the Hu-BRDF correction coefficients for MODIS 0.65- $\mu\text{m}$  band 1<sup>30-31, 32</sup> are used to do the BRDF correction for 0.67- $\mu\text{m}$  RSB M5. In each aggregation zone, a linear regression of reflectance against time is carried out to obtain the slope over the time period 02/2012 to 01/2018. The trend in reflectance is the percentage of change in slope from mission beginning. Fig. 4 shows the trends with the error bars that are calculated from standard deviation of monthly mode reflectances with no BRDF correction (in black), after the BRDF correction in this study (VIIRS BRDF-Cor-Ref; in red), and after the Hu-BRDF correction based on MODIS band 1 (MODIS Hu-BRDF-Cor-Ref; in blue) for M5 for the data from February 2012 and June 2018 in Z1-Z6. The units are in percentage of their corresponding fitted values at the first data point in 02/2012. Both BRDF corrections reduce the standard errors for most zones except for BRDF-Cor-Ref in Z2. The magnitudes of trends are reduced in BRDF-Cor-Ref in all the six zones, and are increased in Hu-BRDF-Cor-Ref except in Z6. The results indicate that the BRDF correction method can reduce the shifts in the long-term reflectance data more effectively than the Hu model based on the MODIS band 1.

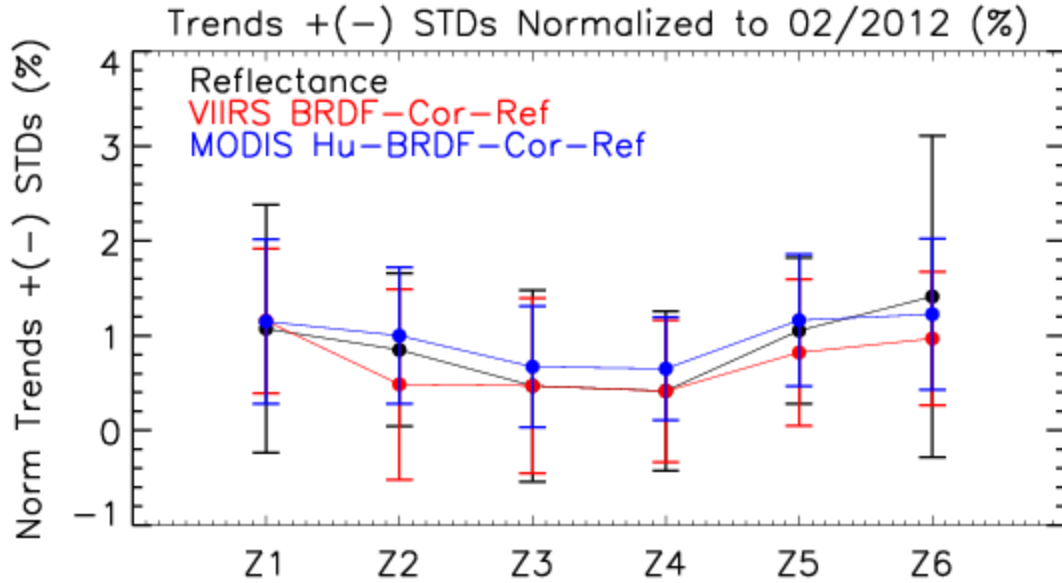


**Fig. 4.** Trends with the uncertainty bars (STDs) of monthly mode reflectances 1) with no BRDF corrections (in black), 2) after the BRDF correction in this study (VIIRS BRDF-Cor-Ref; in red), and 3) after the Hu-BRDF correction based on MODIS band 1 (MODIS Hu-BRDF-Cor-Ref; in blue) normalized to their corresponding fitted values at the first data point in 02/2012 for M5 over 02/2012-06/2018 in the six aggregation zones Z1-Z6.

The time series of normalized reflectance data (in black), the VIIRS BRDF-corrected reflectance data (in red) and the MODIS Hu-corrected reflectance data (in blue) during 02/2012 and 06/2018 in Z3 are compared as an example to show the performance of the BRDF correction methods in Fig. 5. The STD and trend are labeled in Fig. 5 for each dataset. Both BRDF corrections reduce the standard error in DCC reflectances. The Hu-BRDF correction based on MODIS band 1 decreases the STD from 1.01% to 0.64% and to 0.92% by the empirical BRDF in this study. However, the trend after Hu-BRDF correction increases from 0.47% to 0.67%. This indicates that, the Hu-BRDF correction model can reduce the uncertainty in reflectance but can affects the long-term stability in band M5. The difference between these two BRDF-corrected reflectances might be caused by these reasons. (1) The data sources used to derive the BRDF correction coefficients are different. The data source for the BRDF coefficients is from SNPP

VIIRS SDR reflectance product, and from MODIS band 1 for Hu-BRDF correction. There might be system shifts between two reflectance products at 0.65  $\mu\text{m}$ . (2) The two BRDF models use different methods to derive the BRDF coefficients and to apply the BRDF coefficients. The method for the BRDF correction is empirical as described in Section 2. The Hu-MODIS correction is based on Hu et al.'s method<sup>31</sup>. Hu et al.<sup>31</sup> consider the anisotropy factor, the solar zenith dependences of albedo for DCC, and solar irradiance in their model to derive the planetary reflectances. In addition, the Hu-MODIS BRDF coefficients are derived using the MODIS DCC samples at nadir with SZA and VZA less than 40°. (3) There are mismatches in the spectrum between VIIRS RSB M5 and MODIS band 1. The central band wavelength is 0.67  $\mu\text{m}$  for VIIRS M5 and 0.65  $\mu\text{m}$  for MODIS band 1, and the band wavelength width is 20 nm for M5 and 50 nm for MODIS band 1.

In summary, compared to the original monthly mode reflectance, the BRDF correction method in this study proves to be able to reduce the BRDF effects and to evaluate the stability of the SDR products for M5 more effectively than does the Hu-BRDF correction method. Since the Hu-BRDF correction only works for MODIS VIS/NIR bands<sup>30</sup> and there is difference in spectral wavelengths between SNPP VIIRS and MODIS RSB, extending the MODIS-based Hu model correction to other SNPP VIIRS bands is not feasible. Therefore, to assess the stability and to explore the residual RVS effects with minimal impacts from BRDF effects for select RSB in VIIRS SDR reflectance products, the empirical BRDF correction in Section 2 is applied to all VIIRS DCC samples in this study.

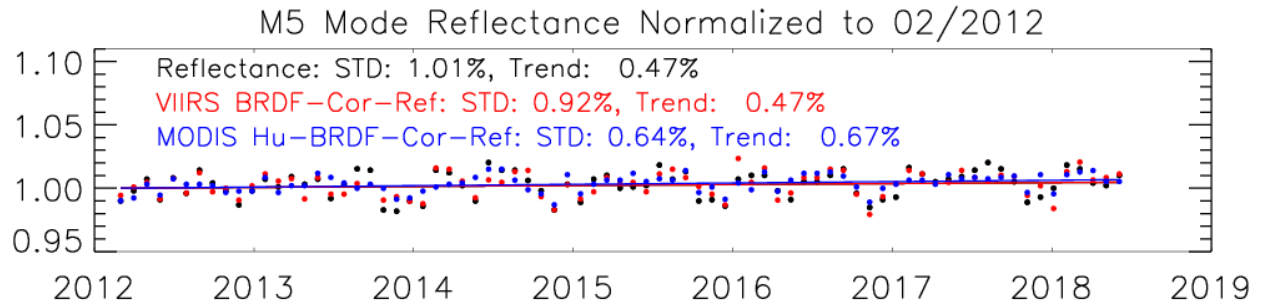


**Fig. 5.** Monthly mode reflectances 1) with no BRDF corrections (in black), 2) after the BRDF correction in this study (VIIRS BRDF-Cor-Ref; in red), and 3) after the Hu-BRDF correction based on MODIS band 1 (MODIS-Hu-BRDF-Cor-Ref; in blue) normalized to their corresponding fitted value at the first data point in 02/2012 for M5 during 02/2012 and 06/2018 in zone 3. The solid lines are the normalized linearly fitted reflectances.

### 3.1.2 Comparison of Reflectance and BRDF-Corrected Reflectance

To check if the BRDF correction improves the reflectance over DCC, the trends and STDs of reflectances and BRDF-corrected reflectances over DCC are compared in Fig. 6. The BRDF correction results in a more stable result by reducing the magnitudes of trends. Furthermore, the standard errors in DCC reflectances for most bands in most zones, especially in the edge zones such as Z1-Z2 and Z5-Z6 are also reduced. The BRDF effects in the nadir zones Z3-Z4 are not as significant as in the edge. The specifications for the calibration accuracy at typical scenes is 2% for M1-11 and I1-3<sup>6</sup>. The trends and standard errors after the BRDF correction are less than 2% in all zones for most RSB. The results indicate that the BRDF-corrected reflectances satisfy the specifications for the calibration accuracy, except band M9. The BRDF-corrected reflectance is used to assess the residual RVS effects in subsection 3.2.

Fig. 6 also shows that the largest fluctuations in monthly mode reflectances are with the SWIR bands M9-11 and I3 before and after the BRDF correction. M8 is a SWIR band but it has the low fluctuations in reflectance as those for other VIS/NIR bands. The standard errors for M9

are larger than 2%, the specified accuracy specification. There are several reasons for the high fluctuations in long-term reflectances for M9-11 and I3, but low fluctuations for M8.

1) The particle size and optical depth in the clouds have the largest impacts on reflectance for the SWIR bands M10 and I3 at 1.61  $\mu\text{m}$  and M11 at 2.25  $\mu\text{m}$ , followed by M9 at 1.378  $\mu\text{m}$ , and the least impacts on the other RSB<sup>33, 35-36</sup>. There is geographic variability in particle size and optical depth<sup>33</sup>. Low optical depth can correspond to thin clouds with large particle size<sup>33-34</sup>. The uncertainty specification 0.07 K in BT in M15<sup>2, 10</sup> can misclassify other clouds as DCC with varying cloud temperatures. As shown in Fig. 2, the BT from M15 over DCC can be as low as 185 K or even lower, resulting in a large range in DCC temperatures, and hence particle sizes and optical depth. The effective ice particle sizes in DCC decrease with cloud temperatures<sup>34</sup>. Generally, smaller particles in DCC have higher reflectances<sup>35</sup>. The variations in cloud particle sizes and optical depth induce the largest uncertainty in reflectance over DCC for M10-M11 and I3, followed by M9, and the least for M8 and other VIS/NIR bands.

2) The spectrum of M9 is similar to MODIS band 26 at 1.378  $\mu\text{m}$ , which are both designed for cirrus cloud detection. The 1.378- $\mu\text{m}$  VIIRS M9 is a strong water vapor absorption band as MODIS band 26<sup>35-36</sup>. In the DCC identification, using a lower BT11 threshold is more reliable to detect convective cloud cores than using a higher BT11 threshold<sup>33-34</sup>. The convective cores of DCC contain less water vapor than the DCC edges and cirrus clouds misidentified as DCC. The variations in water vapor volume in DCC cause significant noise in reflectance over DCC for M9 due to the strong water vapor absorption to the radiance<sup>36</sup>. The impacts of fluctuated water vapor volume on the reflectance are insignificant for the 1.61- $\mu\text{m}$  M10 and I3, the 2.25- $\mu\text{m}$  M11, and the 1.24- $\mu\text{m}$  M8<sup>28</sup>. For M9, in most zones, the BRDF correction doesn't change the trends or the errors significantly for M9. The combined impacts on the reflectance from particle



size and atmospheric water vapor absorption induce the largest uncertainties in M9, followed by M10, I3 and M11, and the least uncertainties for M8. The combined impacts from varying atmospheric particle size and water vapor absorption are more significant than the impacts from BRDF effects for M9, hence the BRDF correction doesn't change the stability or the errors much in most zones for M9.

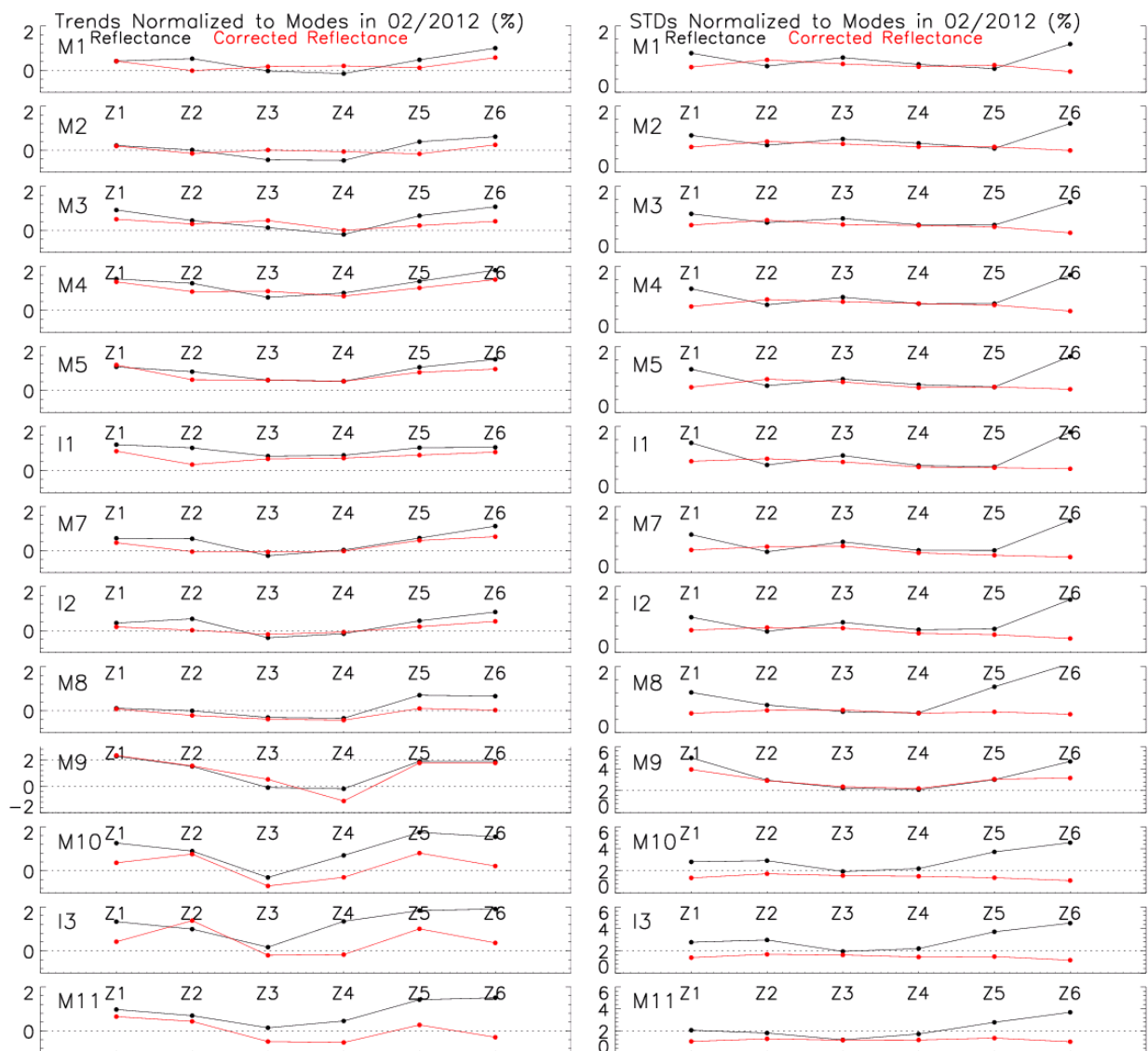


**Fig. 6.** Trends (Left Panel) and STDs (Right Panel) of monthly mode reflectances before (in black) and after (in red) the BRDF correction normalized to their corresponding fitted values at the first data point in 02/2012 for M1-M5,

M7-M11, and I1-I3. The dashed lines in trends represent the zero-trend lines and 2%-trend line for M9. The dashed lines in STDs represent the 2%-STD lines for the SWIR bands M9-M11 and I3.

## *3.2 RVS Effect Assessment*

### *3.2.1 Scan Angles Dependency*

The HAM has a scan-angle-dependent AOI variation from  $29.0^{\circ}$  to  $56.6^{\circ}$  over the full EV scan angle. The frames in the VIIRS SDR products correspond to the HAM AOIs<sup>18, 27</sup>. To explore the residual RVS effects in the SDR reflectance products, the 750-m DCC samples for M-bands and aggregated I-bands are divided into the six aggregation zones Z1-Z6 according to the frame numbers as shown in Table 2.

As described in 2.2.1, reflectance in M5 for M-bands and reflectance in I1 for I-bands are combined with brightness temperature in M15 to identify DCC samples. The monthly numbers of DCC samples for M5 in the six aggregation zones are shown in Fig. 7. There are sufficient DCC samples (more than one million) for each month and each frame zone. The temporal trend in DCC numbers is negligible in each zone and the seasonal fluctuations in the DCC number are similar in Z1-Z6. The DCC sample sizes are close in the four middle zones Z2-Z5. However, the DCC sample sizes are larger in the two end zones Z1 and Z6 than in others. In the VIIRS SDR product nadir Z3-Z4, three detectors along scan with a horizontal resolution of 0.259 km are aggregated to form a single VIIRS pixel for M5<sup>27</sup>. In Z2 and Z5, two detectors are integrated into one VIIRS pixel. At either end of a scan in a granule, the footprint of the pixel size along track by cross track is 1.60 km by 1.58 km for M5. In addition, three-dimensional cloud effects on the observed radiance dramatically increase for oblique views, especially for DCC<sup>37</sup>. The satellite cloud optical thickness retrievals are much higher under oblique views than under overhead views if clouds are inhomogeneous. The radiative effect of cloud sides viewed at

oblique angles contributes most to the enhanced optical thickness values<sup>38</sup>. The increase in optical thickness results in higher reflectance and lower 11- $\mu$ m brightness temperature. These are the possible reasons for the increase in the DCC sample sizes at the two end frame zones Z1 and Z6.

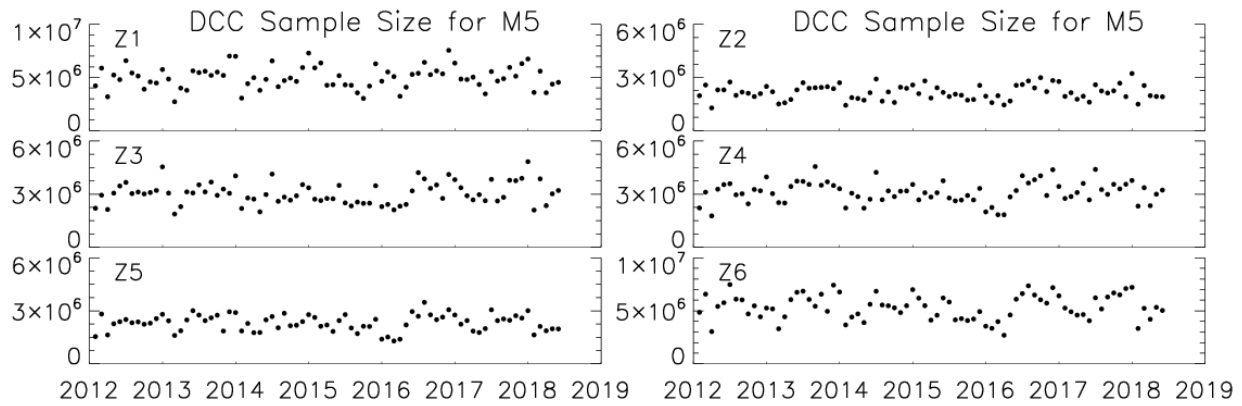


**Fig. 7.** Numbers of monthly DCC samples in the six frame zones for M5 during February 2012 and May 2017. Z1: frames 1-640 for zone 1; Z2: frames 641-1008 for zone 2; Z3: frames 1009-1600 for zone 3; Z4: frames 1601-2192 for zone 4; Z5: frames 2193-2560 for zone 5; Z6: frames 2561-3200 for zone 6. The solid lines are the linearly fitted DCC sample numbers.

### 3.2.2 RVS Effect Assessment Using DCC

The BRDF effects affect the reflectance with larger AOIs since BRDF specifies the behavior of surface scattering as a function of illumination and view angles at a particular wavelength<sup>28</sup>. The comparison of trends and errors in reflectance before and after the BRDF correction shown in Fig. 6 indicates that, the application of the BRDF correction improves the stability by reducing the trends and reduces the standard errors of reflectances for most RSB except for M9 in Z1-Z6. The reductions in the standard errors by BRDF correction are most significant at the edge zones Z1 and Z6 for all the RSB including M8 and M9. The time series of BRDF-corrected monthly DCC reflectances with their linear regression lines are shown in Fig. 8, and trends and STDs are listed in Table 3 for all select RSB in the six zones. After the BRDF correction, the difference in

standard errors between the six frame zones is small for each RSB (Fig. 6, Fig. 8, Table 3). This indicates that the BRDF correction can effectively exclude the uncertainty caused by the BRDF effects at different view angles. The BRDF-corrected reflectances over DCC are more precise to detect the residual RVS effects and are used to investigate the residual RVS effects in VIIRS SDR for each RSB in this study.

Fig. 8 and Table 3 indicate that the magnitudes of trends are greater than their corresponding standard errors in DCC reflectances for M4-M5 in Z1 and Z5-Z6, and I1 and M7 in Z6. The RSB calibrations might not be complete for these RSB at these AOIs which require for further attentions in the future calibrations. Substantial ranges in trends exist among different frame zones for most RSB. Since F-factor is the same in all zones for a given band at a given time, the unconsidered change in RVS with time might be the reason for the large variation in trends between different aggregation zones. Currently, the RVS is measured pre-launch. As mission continues, the differences in reflectance drifts caused by the residual RVS will induce higher differences in reflectances between different zones. Further analyses to detect the residual RVS effects in SDR reflectance products are necessary as in the following subsection 3.2.3.

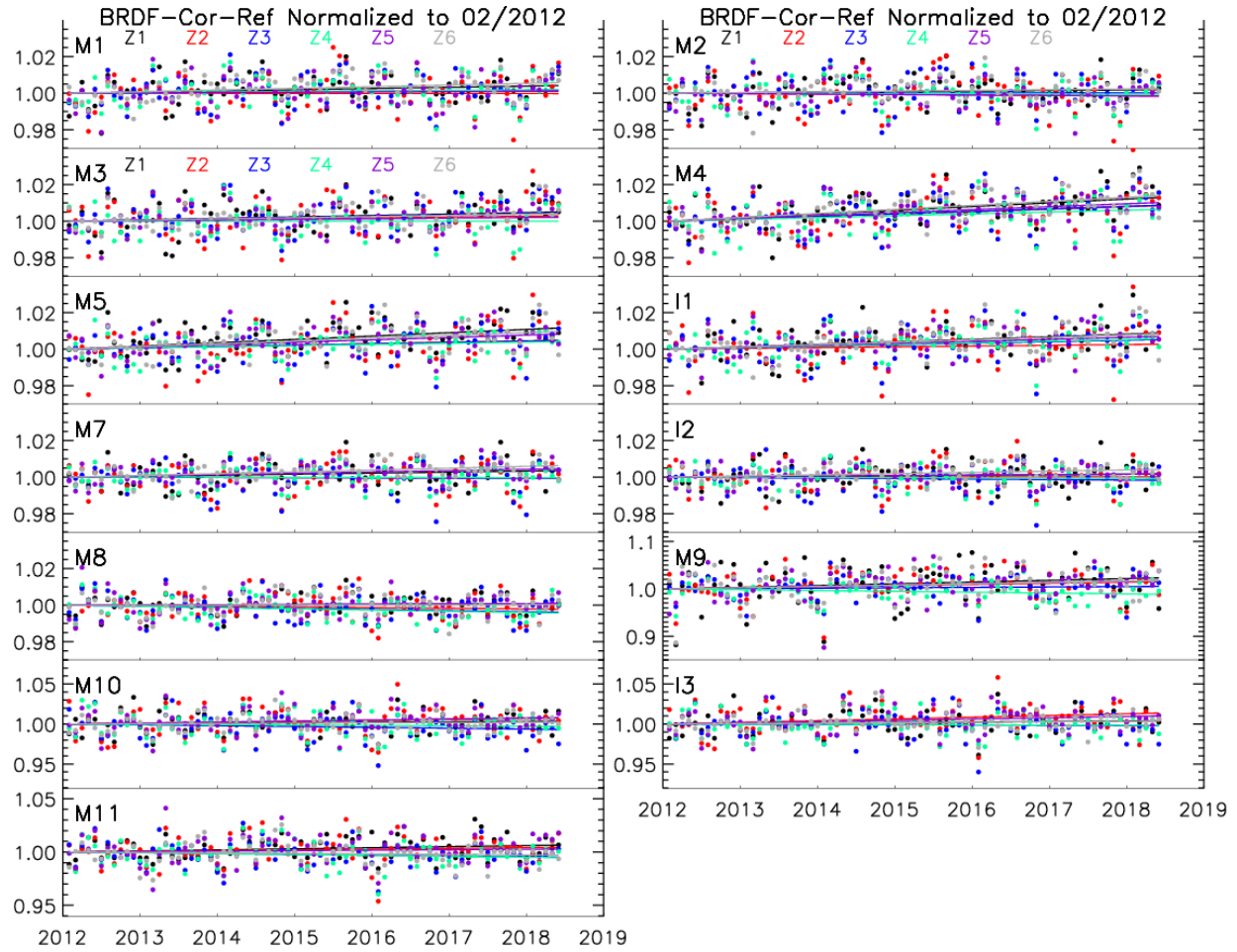


**Fig. 8.** Monthly BRDF-corrected mode reflectances normalized to their corresponding value at the first data point in 02/2012 in the six frame zones for the select RSB during February 2012 and June 2018. The solid lines are the normalized linearly fitted reflectances.

**Table 3** Trends and standard deviations (STDs) of monthly mode reflectances after the BRDF correction (BRDF-Cor-Ref) normalized to their corresponding fitted values at the first data point in 02/2012 for select RSB. Ranges represent for the spans of the trends and STDs among the Z1-Z6 for all bands. The units are in percentage of fitted mode values in 02/2012.

Zone	Trend (STD) (%) in BRDF-Cor-Ref					
	Z1	Z2	Z3	Z4	Z5	Z6
M1	0.41 (0.76)	-0.02 (0.98)	0.16 (0.86)	0.19 (0.77)	0.11 (0.82)	0.57 (0.63)
M2	0.19 (0.77)	-0.14 (0.93)	0.01 (0.86)	-0.06 (0.77)	-0.16 (0.77)	0.25 (0.66)
M3	0.50 (0.83)	0.29 (0.98)	0.45 (0.84)	0.00 (0.81)	0.22 (0.77)	0.41 (0.59)
M4	1.30 (0.78)	0.85 (1.00)	0.87 (0.93)	0.65 (0.88)	1.02 (0.83)	1.40 (0.65)
M5	1.16 (0.76)	0.49 (1.01)	0.47 (0.92)	0.41 (0.75)	0.82 (0.77)	0.97 (0.70)
I1	0.88 (0.95)	0.27 (1.02)	0.52 (0.92)	0.56 (0.77)	0.70 (0.75)	0.83 (0.72)
M7	0.36 (0.68)	-0.05 (0.78)	-0.06 (0.80)	-0.03 (0.60)	0.46 (0.52)	0.63 (0.47)

I2	0.17 (0.68)	0.02 (0.76)	-0.17 (0.74)	-0.07 (0.59)	0.18 (0.54)	0.42 (0.43)
M8	0.08 (0.59)	-0.22 (0.68)	-0.39 (0.69)	-0.43 (0.59)	0.10 (0.63)	0.02 (0.56)
M9	2.34 (3.93)	1.55 (2.91)	0.53 (2.37)	-1.11 (2.20)	1.77 (3.05)	1.77 (3.15)
M10	0.36 (1.35)	0.75 (1.73)	-0.69 (1.56)	-0.30 (1.50)	0.80 (1.37)	0.22 (1.12)
I3	0.41 (1.38)	1.37 (1.69)	-0.20 (1.62)	-0.17 (1.44)	1.00 (1.48)	0.36 (1.16)
M11	0.65 (1.04)	0.43 (1.28)	-0.49 (1.15)	-0.53 (1.17)	0.27 (1.34)	-0.29 (1.01)

### 3.2.3 Comparison of Residual RVS Effects between DCC and Deserts

To evaluate the assessment results from DCC samples, the reflectances from 13 different frames over selected desert sites Libya 2 (25.05°N, 20.48°E), Libya 4 (28.55°N, 23.39°E) and Egypt 1 (27.12°N, 26.10°E) in the Northern African region are compared with those over DCC. The 13 frames are 295, 432, 775, 1000, 1260, 1442, 1640, 1830, 2002, 2095, 2245, 2747, and 2920, respectively. The frame numbers and corresponding desert site names are listed in Table 4. At each desert frame, the reflectance data in a 20 by 20 km window centered at the specific desert site are collected and averaged at each HAM side from repeatable orbits every 16 days. A semi-empirical BRDF model based on Roujean et al.<sup>39</sup> is used with site-specific coefficients determined from the data over the first three years of mission (Wu et al., 2017). The BRDF corrected reflectances are used to track the stability over the 13 frames. A linear fit is applied to the data at each frame to determine the overall drift. The SWIR band M9 is not monitored using desert data due to the strong water vapor absorption effects. Since the uncertainty in DCC reflectance is large, between 2-4%, for M9 as listed in Table 3, the residual RVS effects on M9 are not explored in the following study.

**Table 4** The corresponding desert site names (Sites) for the 13 desert frames (FR).

Sites	Libya 2	Libya 4	Egypt 1
FR	295, 1000, 2747, 2920	432, 775, 1260, 1442, 1640, 1830, 2002	2095, 2245

The ranges of frames, scan angles, and AOIs for Z1-Z6 in the SDR product are listed in Table 2. Except for only one frame 2245 at Egypt 1 is covered in the frame range for Z5, at least two desert frames are covered in each of the other aggregation zones. At each frame for each band, the trend is calculated as the percentage of change in the linearly fitted reflectance at 06/2018 to that at 02/2012. The temporal trends and fluctuations in reflectances at different desert frames (in red) are compared with those over DCC (in black) as shown in Fig. 9. The trends with the STD bars over DCC overlap with those at desert sites in the same zone. This indicates that the desert stability assessment results agree with those from the DCC. Except for M10 and I3 which is affected by the varying particle sizes in clouds the most, DCC reflectances in each zone have less uncertainties than those at the neighboring desert sites in the same frame zone for all the other RSB. This indicates that the DCC results are more reliable than those from the deserts for most RSB except for M10 and I3. In Fig. 9, the magnitudes of trends in desert reflectances for M2 in Z3, M3 in Z4, M4 in Z1, M5 in Z1 and Z6, M7 in Z3 and Z6, M8 in Z3, M10 and I3 in Z2-Z4, I1-I2 in Z6 are greater than their corresponding standard errors. The calibration for these RSB in these zones might not be completed and require for more attentions in future calibrations.

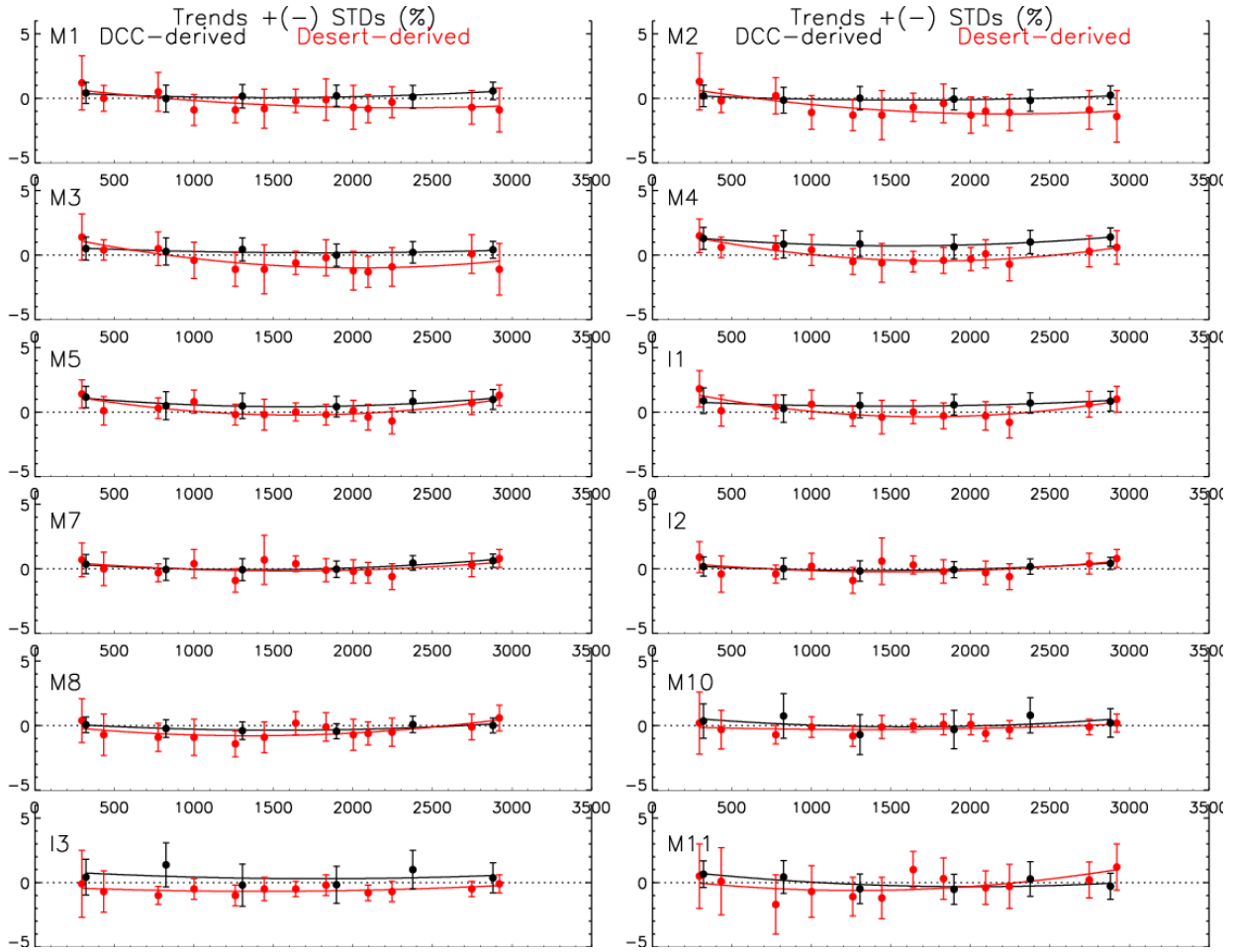
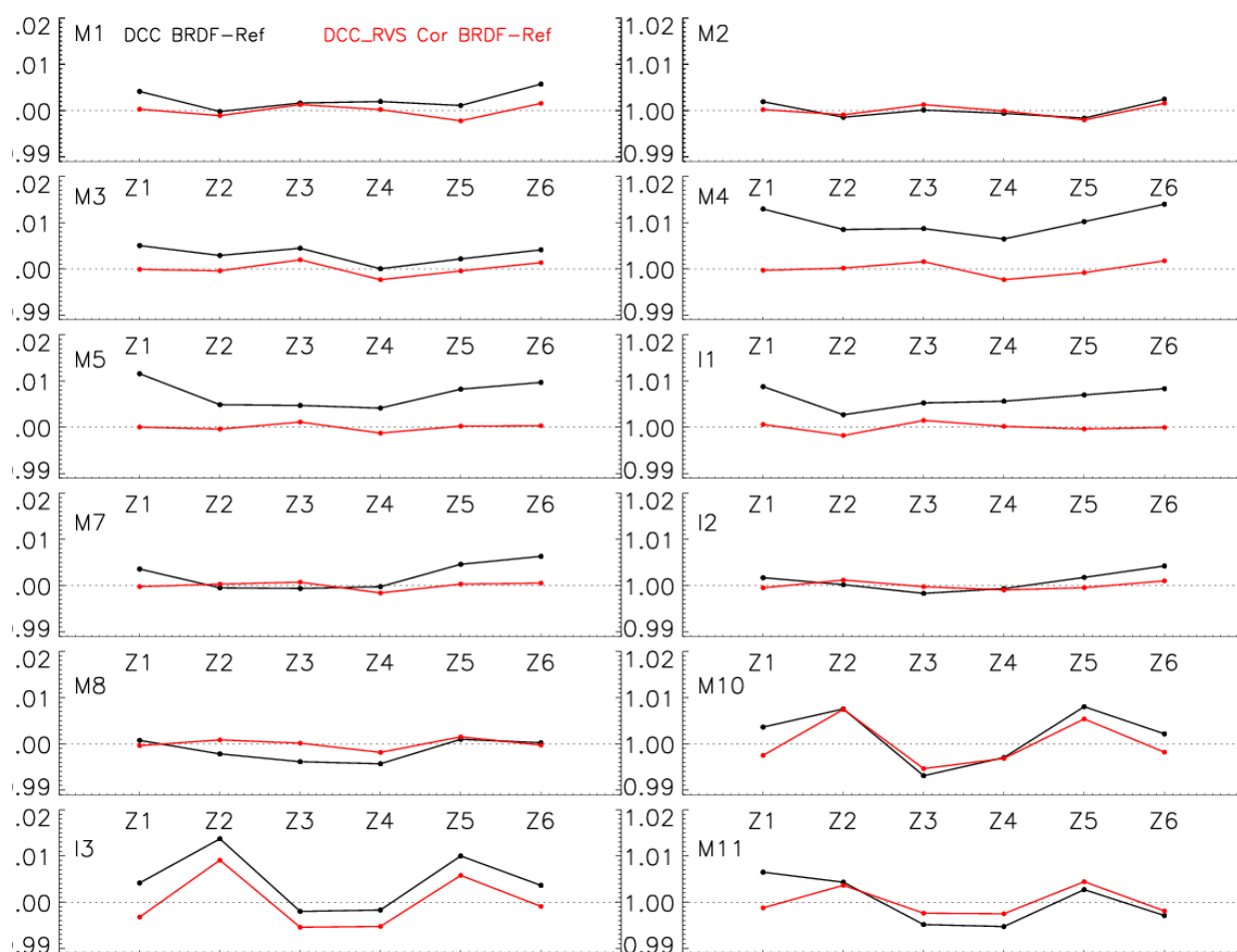


**Fig. 9.** Trends with the uncertainty bars (STDs) of monthly BRDF-corrected mode reflectances at 06/2018 along frames. The solid lines are the quadratic fitted trends against AOIs from DCC in black and from deserts in red for M1-M5, M7-M8, M10-M11, and I1-I3. The units are in percentage of fitted mode values in 02/2012.

A quadratic fitting is applied to the trends at 06/2018 against AOIs over the six zones from DCC and over the 13 desert frames from desert sites, respectively. Fig. 9 implies that the observed trends are evenly distributed beside the quadratic fitted lines along AOI from DCC and from deserts. The trends vary along AOIs and the trends with STD bars overlap at different AOIs. To evaluate the residual RVS effects on reflectance, a time and AOI dependent function, named DCC-RVS and Desert-RVS, is derived by applying a quadratic fit (as a function of AOI) to the linearly fitted reflectances from each site normalized to 02/2012. The reflectance is RVS corrected as divided by the RVS at a given time. Fig. 10 shows the reflectance from DCC before



444 (DCC BRDF-Ref) and after the correction by the DCC-derived RVS (DCC-RVS Corr BRDF-  
 445 Ref) as of June, 2018. The RVS correction improves the stability and reduces the differences in  
 446 most zones for all the RSB including M9 (not shown). The RVS effects are most significant for  
 447 the VIS/NIR bands M3-M5, M7 and I1. Fig. 11 shows the normalized reflectances from deserts  
 448 before (Desert BRDF-Ref) and after the correction by the desert-derived RVS (Desert-RVS Corr  
 449 BRDF-Ref) as of June, 2018. The correction by the desert-RVS reduces the reflectance trends  
 450 from desert sites at most frames. The difference in reflectances at different frames is reduced.  
 451 The RVS correction from deserts are most significant for bands M1-M4. This indicates that  
 452 considering time-dependent RVS might improve the long-term stability of the VIIRS data and  
 453 also reduce the deviations in reflectance observed at different AOIs.



454

**Fig. 10.** Reflectance from DCC before (DCC BRDF-Ref, in black) and after the correction by the DCC-derived RVS (DCC-RVS Corr BRDF-Ref, in red) against frame numbers over the six zones for M1-M5, M7-M8, M10-M11, and I1-I3. The units are in percentage of fitted reflectance values in 02/2012.

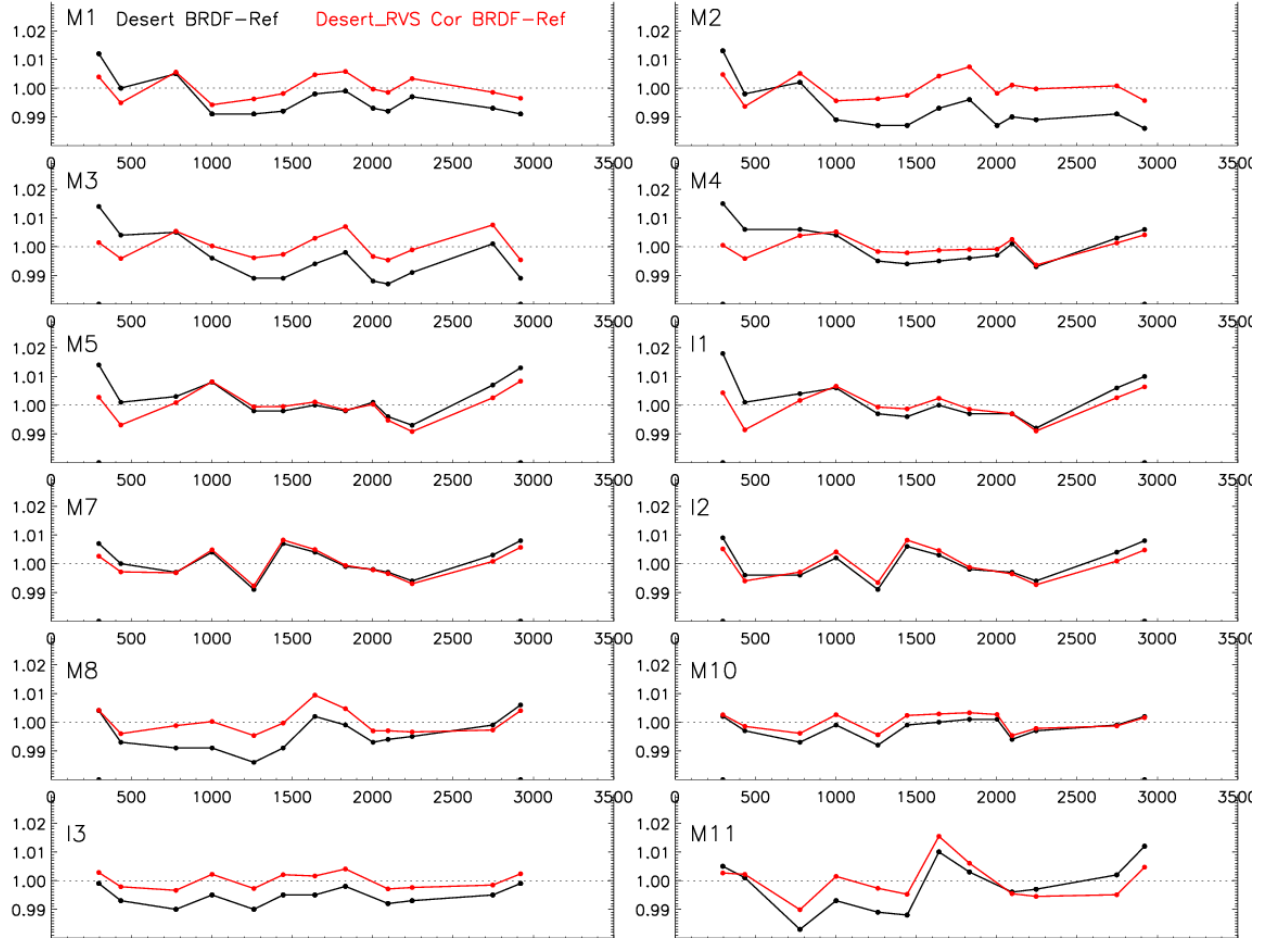


**Fig. 11.** Reflectance from deserts before (Desert BRDF-Ref, in black) and after the correction by the desert-derived RVS (Desert-RVS Corr BRDF-Ref, in red) against frame numbers over the 13 frames for M1-M5, M7-M8, M10-M11, and I1-I3. The units are in percentage of fitted reflectance values in 02/2012.

## 4 Conclusions

In this study, the performance of VIIRS calibrations for SDR reflectance product is assessed using DCCT for 10 M-bands (M1-M5 and M7-M11) and three I-bands (I1-I3) over 02/2012-06/2018. An empirical BRDF correction is applied to SDR reflectance data over DCC and reduces the STD difference between different AOIs. The empirical BRDF correction method

reduces the uncertainty in reflectance and increases the stability of the reflectance products for most RSB. The BRDF-corrected reflectances are used in this study to evaluate the stability of the VIIRS SDR reflectance products and to explore the residual RVS effects at different AOIs. The major findings about the stability assessment and RVS effect exploration from this study include the following.

1. The reflectance trends satisfy the specifications for the calibration accuracy for most bands. However, the magnitudes of trends are marginally greater than their corresponding standard errors in DCC reflectances for M4-M5 in Z1 and Z5-Z6, and I1 and M7 in Z6, and in desert reflectances for M2 in Z3, M3 in Z4, M4 in Z1, M5 in Z1 and Z6, M7 in Z3 and Z6, M8 in Z3, M10 and I3 in Z2-Z4, I1-I2 in Z6. The RSB calibration might not be adequate at these AOIs and requires for further understanding.

2. The desert stability assessment results agree with those observed from the DCC. DCC reflectance in each aggregation zone has less uncertainty than desert sites in the same frame zone for all the RSB except for M10 and I3 which are most affected by the varying particle sizes in clouds. This indicates that the DCC results are more reliable than those from the deserts for most RSB except for M10 and I3.

3. The residual RVS function is derived as a quadratic fit of reflectance against AOIs at a given time. The RVS correction improves the stability and reduces the differences at different AOIs for all the RSB, especially for the VIS/NIR bands M3-M5, M7 and I1 using the DCC method.

In summary, the BRDF correction can effectively reduce the BRDF effects on DCC reflectances. BRDF-corrected reflectances over DCC should be utilized in the future operational stability assessments and RVS effect assessment for VIIRS SDR products. BRDF corrected DCC

reflectances are more stable compared to BRDF corrected desert observations and are recommended for stability assessment and residual RVS exploration. As mission continues, the differences in trends from different AOIs will result in larger differences in reflectances. Continuing monitoring of on-orbit RVS stability and its effects on VIIRS SDR reflectance product is necessary with the DCC approach in the future calibration consideration.

## *References*

1. Cao, C., De Luccia, F.J., Xiong, X., Wolfe, R. and Weng, F., 2014. Early on-orbit performance of the visible infrared imaging radiometer suite onboard the suomi national polar-orbiting partnership (S-NPP) satellite. *IEEE Transactions on Geoscience and Remote Sensing*, 52(2), pp.1142-1156.
2. Cao, C., Xiong, X., Wolfe, R., De Luccia, F., Liu, Q., Blonski, S., Lin, G., Nishihama, M., Pogorzala, D., Oudrari, H. and Hillger, D., 2013. Visible Infrared Imaging Radiometer Suite (VIIRS) Sensor Data Record (SDR) User's Guide. NOAA Technical Report NESDIS: College Park, MD, USA.
3. Holben, B.N., Kaufman, Y.J. and Kendall, J.D., 1990. NOAA-11 AVHRR visible and near-IR inflight calibration. *International Journal of Remote Sensing*, 11(8), pp.1511-1519.
4. Kramer, H.J., 2002. *Observation of the Earth and its Environment: Survey of Missions and Sensors*. Springer Science & Business Media.
5. Guenther, B., Xiong, X., Salomonson, V.V., Barnes, W.L. and Young, J., 2002. On-orbit performance of the Earth Observing System Moderate Resolution Imaging Spectroradiometer; first year of data. *Remote Sensing of Environment*, 83(1-2), pp.16-30.
6. Moyer, D., McIntire, J., Oudrari, H., McCarthy, J., Xiong, X. and De Luccia, F., 2016. JPSS-1 VIIRS pre-launch response versus scan angle testing and performance. *Remote Sensing*, 8(2), p.141.
7. Lei, N., Wang, Z., Fulbright, J., Lee, S., McIntire, J., Chiang, K. and Xiong, X., 2012, October. Initial on-orbit radiometric calibration of the Suomi NPP VIIRS reflective solar bands. In *Earth Observing Systems XVII* (Vol. 8510, p. 851018). International Society for Optics and Photonics.

8. Cardema, J.C., Rausch, K.W., Lei, N., Moyer, D.I. and De Luccia, F.J., 2012, October. Operational calibration of VIIRS reflective solar band sensor data records. In Earth Observing Systems XVII (Vol. 8510, p. 851019). International Society for Optics and Photonics.
9. Sun, J. and Wang, M., 2015. On-orbit calibration of Visible Infrared Imaging Radiometer Suite reflective solar bands and its challenges using a solar diffuser. *Applied optics*, 54(24), pp.7210-7223.
10. Xiong, X., Butler, J., Chiang, K., Efremova, B., Fulbright, J., Lei, N., McIntire, J., Oudrari, H., Sun, J., Wang, Z. and Wu, A., 2014. VIIRS on-orbit calibration methodology and performance. *Journal of Geophysical Research: Atmospheres*, 119(9), pp.5065-5078.
11. Xiong, X., Sun, J., Fulbright, J., Wang, Z. and Butler, J.J., 2016. Lunar calibration and performance for S-NPP VIIRS reflective solar bands. *IEEE Transactions on Geoscience and Remote Sensing*, 54(2), pp.1052-1061.
12. Lei, N. and Xiong, X., 2017. Impacts of the Angular Dependence of the Solar Diffuser BRDF Degradation Factor on the SNPP VIIRS Reflective Solar Band On-Orbit Radiometric Calibration. *IEEE Transactions on Geoscience and Remote Sensing*, 55(3), pp.1537-1543.
13. Haas, E., Moyer, D., De Luccia, F., Rausch, K. and Fulbright, J., 2012, October. VIIRS solar diffuser bidirectional reflectance distribution function (BRDF) degradation factor operational trending and update. In Earth Observing Systems XVII (Vol. 8510, p. 851016). International Society for Optics and Photonics.
14. Fulbright, J., Lei, N., Efremova, B. and Xiong, X., 2016. Suomi-NPP VIIRS Solar Diffuser Stability Monitor Performance. *IEEE Trans. Geoscience and Remote Sensing*, 54(2), pp.631-639.
15. Lei, N. and Xiong, X., 2016. Suomi NPP VIIRS solar diffuser BRDF degradation factor at short-wave infrared band wavelengths. *IEEE Transactions on Geoscience and Remote Sensing*, 54(10), pp.6212-6216.
16. Baker, N. and Kilcoyne, H., 2013. Joint Polar Satellite System (JPSS) VIIRS Radiometric Calibration Algorithm Theoretical Basis Document ATBD. rev. C; Goddard Space Flight Center, Greenbelt, MD, pp.163-165.

17. Sun, J., Xiong, X., Angal, A., Chen, H., Wu, A. and Geng, X., 2014. Time-dependent response versus scan angle for MODIS reflective solar bands. *IEEE Transactions on Geoscience and Remote Sensing*, 52(6), pp.3159-3174.
18. Sun, J. and Wang, M., 2016. VIIRS reflective solar bands calibration progress and its impact on ocean color products. *Remote Sensing*, 8(3), p.194.
19. Bhatt, R., Doelling, D.R., Wu, A., Xiong, X., Scarino, B.R., Haney, C.O. and Gopalan, A., 2014. Initial stability assessment of S-NPP VIIRS reflective solar band calibration using invariant desert and deep convective cloud targets. *Remote Sensing*, 6(4), pp.2809-2826.
20. Chang, T., Xiong, X. and Mu, Q., 2016. VIIRS Reflective Solar Band Radiometric and Stability Evaluation Using Deep Convective Clouds. *IEEE Transactions on Geoscience and Remote Sensing*, 54(12), pp.7009-7017.
21. Bhatt, R., Doelling, D.R., Scarino, B., Haney, C. and Gopalan, A., 2017. Development of Seasonal BRDF Models to Extend the Use of Deep Convective Clouds as Invariant Targets for Satellite SWIR-Band Calibration. *Remote Sensing*, 9(10), p.1061.
22. Wang, W., C. Cao (2015) DCC radiometric sensitivity to spatial resolution, cluster size, and LWIR calibration bias based on VIIRS observations. *Journal of Atmospheric and Oceanic Technology*, 32(1), pp.48-60.
23. Wang, W. and Cao, C., 2016. Monitoring the NOAA operational VIIRS RSB and DNB calibration stability using monthly and semi-monthly deep convective clouds time series. *Remote Sensing*, 8(1), p.32.
24. Uprety, S. and Cao, C., 2015. Suomi NPP VIIRS reflective solar band on-orbit radiometric stability and accuracy assessment using desert and Antarctica Dome C sites. *Remote Sensing of Environment*, 166, pp.106-115.
25. Wu, A., Xiong, X.J. and Cao, C., 2017, September. Assessment of stability of the response versus scan angle for the S-NPP VIIRS reflective solar bands using pseudo-invariant desert and Dome C

565 sites. In Sensors, Systems, and Next-Generation Satellites XXI (Vol. 10423, p. 1042322).  
 566 International Society for Optics and Photonics.

567 26. Mu, Q., Chang, T., Wu, A., Xiong, X., 2018. Evaluating the Long-term Stability and Response versus  
 568 Scan Angle Effect in the SNPP VIIRS SDR Reflectance Product Using a Deep Convective Cloud  
 569 Technique. In Proceedings of the Optical Science and Technology, SPIE Defense + Security.  
 570 International Society for Optics and Photonics.

571 27. Baker, N., 2011. Joint polar satellite system (JPPS) VIIRS geolocation algorithm theoretical basis  
 572 document (ATBD). NASA Goddard Space Flight Center Tech. Doc, pp.474-00053.

573 28. Schaaf, C.B., Gao, F., Strahler, A.H., Lucht, W., Li, X., Tsang, T., Strugnell, N.C., Zhang, X., Jin, Y.,  
 574 Muller, J.P. and Lewis, P., 2002. First operational BRDF, albedo nadir reflectance products from  
 575 MODIS. Remote sensing of Environment, 83(1-2), pp.135-148.

576 29. Doelling, D.R., Nguyen, L. and Minnis, P., 2004, October. On the use of deep convective clouds to  
 577 calibrate AVHRR data. In Earth Observing Systems IX (Vol. 5542, pp. 281-290). International  
 578 Society for Optics and Photonics.

579 30. Mu, Q., Wu, A., Xiong, X., Doelling, D.R., Angal, A., Chang, T. and Bhatt, R., 2017. Optimization  
 580 of a Deep Convective Cloud Technique in Evaluating the Long-Term Radiometric Stability of  
 581 MODIS Reflective Solar Bands. Remote Sensing, 9(6), p.535.

582 31. Hu, Y., Wielicki, B.A., Yang, P., Stackhouse, P.W., Lin, B. and Young, D.F., 2004. Application of  
 583 deep convective cloud albedo observation to satellite-based study of the terrestrial atmosphere:  
 584 Monitoring the stability of spaceborne measurements and assessing absorption anomaly. IEEE  
 585 transactions on geoscience and remote sensing, 42(11), pp.2594-2599.

586 32. Doelling, D.R., Morstad, D., Bhatt, R. and Scarino, B., 2011. Algorithm theoretical basis document  
 587 (ATBD) for deep convective cloud (DCC) technique of calibrating GEO sensors with Aqua-MODIS  
 588 for GSICS. GSICS.

33. Doelling, D.R., Morstad, D., Scarino, B.R., Bhatt, R. and Gopalan, A., 2013. The characterization of deep convective clouds as an invariant calibration target and as a visible calibration technique. IEEE transactions on Geoscience and remote Sensing, 51(3), pp.1147-1159.
34. Hong, G., Minnis, P., Doelling, D., Ayers, J.K. and Sun-Mack, S., 2012. Estimating effective particle size of tropical deep convective clouds with a look-up table method using satellite measurements of brightness temperature differences. Journal of Geophysical Research: Atmospheres, 117(D6).
35. King, M.D., S.C. Tsay, S.E. Platnick, M. Wang, K.N. Liou, 2011. Cloud Retrieval Algorithms for MODIS: Optical Thickness, Effective Particle Radius, and Thermodynamic Phase. [https://cimss.ssec.wisc.edu/dbs/China2011/Day2/Lectures/MOD06OD\\_Algorithm\\_Theoretical\\_Basis\\_Document.pdf](https://cimss.ssec.wisc.edu/dbs/China2011/Day2/Lectures/MOD06OD_Algorithm_Theoretical_Basis_Document.pdf).
36. Godin, R., 2014. Joint Polar Satellite System (JPSS) VIIRS Cloud Effective Particle Size and Cloud Optical Thickness Algorithm Theoretical Basis Document (ATBD). Goddard Space Flight Center Greenbelt, Maryland.
37. Angal, A., Xiong, X., Mu, Q., Doelling, D.R., Bhatt, R. and Wu, A., 2017. Results From the Deep Convective Clouds-Based Response Versus Scan-Angle Characterization for the MODIS Reflective Solar Bands. IEEE Transactions on Geoscience and Remote Sensing.
38. Várnai, T. and Marshak, A., 2007. View angle dependence of cloud optical thicknesses retrieved by Moderate Resolution Imaging Spectroradiometer (MODIS). Journal of Geophysical Research: Atmospheres, 112(D6).
39. Roujean, J.L., Leroy, M. and Deschamps, P.Y., 1992. A bidirectional reflectance model of the Earth's surface for the correction of remote sensing data. Journal of Geophysical Research: Atmospheres, 97(D18), pp.20455-20468.

### *Acknowledgment*

We would like to show our gratitude to our colleague Amit Angal for his great suggestions and comments to this research. Special thanks are given to David R. Doelling and Rajendra Bhatt for



614 providing the MODIS band 1 Hu-BRDF coefficients. We are grateful to Ning Lei and Xuexia  
615 Chen for their helpful consultations on VIIRS RSB calibrations. This study is an improvement to  
616 the work presented in “Mu, Q., Chang, T., Wu, A., Xiong, X., 2018. Evaluating the Long-term  
617 Stability and Response versus Scan Angle Effect in the SNPP VIIRS SDR Reflectance Product  
618 Using a Deep Convective Cloud Technique. In Proceedings of the Optical Science and  
619 Technology, SPIE Defense + Security. International Society for Optics and Photonics.”

620  
621 **Qiaozhen Mu** received the B.S. degree in Physics and the M.S. degree in Geography from Beijing  
622 Normal University, China, in 1995 and 1998, respectively. She received the Ph.D. degree in  
623 Climatology from Peking University China, in 2001. Qiaozhen Mu is currently with the Science  
624 Systems and Applications, Inc., Lanham, MD, USA, involved in the Moderate Resolution  
625 Imaging Spectroradiometer (MODIS) Characterization and Support Team, National Aeronautics  
626 and Space Administration, Goddard Space Flight Center, Greenbelt, MD, USA. She is involved  
627 in the radiometric calibration and validation of MODIS sensor, and the assessments of  
628 calibration performance of MODIS and VIIRS Level 1B products.



630 **Xiaoxiong (Jack) Xiong** received the B.S. degree in optical  
631 engineering from the Beijing Institute of Technology, Beijing, China, and the Ph.D. degree in  
632 physics from the University of Maryland, College Park.

He is an optical physicist at the National Aeronautics and Space Administration (NASA),  
Goddard Space Flight Center (GSFC), currently serving as the MODIS Project Scientist and the  
Technical Lead for both the MODIS Characterization Support Team (MCST) and the VIIRS  
Characterization Support Team (VCST). Before joining the NASA/GSFC, he had also worked in  
the fields of optical instrumentation, nonlinear optics, laser and atomic spectroscopy, and  
resonance ionization mass spectrometry at universities, industry, and the National Institute of  
Standards and Technology (NIST).



**Tiejun Chang** received a M.S. degree in Computer Science from Montana  
State University, and a Ph.D degree in Optics from University of Paris-Sud, France. His work  
focuses on radiometric calibration and validation of satellite remote sensor and has experience on  
MODIS, VIIRS, AVHRR, and GOES-R/ABI. He is working with MODIS and VIIRS  
Characterization and Support Teams at the National Aeronautics and Space Administration  
(NASA), Goddard Space Flight Center (GSFC).



**Aisheng Wu** received the B.S. degree in atmospheric science from the University of Science and Technology of China, Hefei, China, and the M.Sc. degree in atmospheric remote sensing from the Chinese Academy of Science, Institute of Plateau Atmospheric Physics, Lanzhou, China, and the Ph.D. degree in biometeorology/soil physics from the University of British Columbia, Vancouver, BC, Canada. Currently he is with both MODIS and Visible Infrared Imaging Radiometer Suite (VIIRS) Characterization and Support Teams at the National Aeronautics and Space Administration (NASA), Goddard Space Flight Center (GSFC).

### **Caption List**

**Fig. 1** (a) Schematic diagram of VIIRS onboard calibrations for VIIRS reflective solar bands (RSB); (b) scan angles of VIIRS view sectors and their corresponding Angles of Incidence (AOIs) on the Half Angle Mirror (HAM). SD: Solar Diffuser; SDSM: SD stability monitor; SIS: Spherical Integrating Source; RTA: Rotating Telescope Assembly.

**Fig. 2** Spatial patterns and their corresponding histograms of 11- $\mu$ m moderate resolution band M15 brightness temperature (BT11) for LSIPS VIIRS V5000 SDR granule 2014305.0500 on 11/01 2014 using: all valid frames (a, b); potential deep convective cloud (DCC) frames (c, d) and DCC frames (e, f) with BT11 less than 210 K before and after the spatial uniformity test, respectively. Gray color in the spatial maps represents pixels with filled value.

**Fig. 3.** Monthly probability distribution functions (PDF) of reflectance before (Left Panel) and after the BRDF correction (Right Panel) over DCC for M5 (a, b) and I1 (c, d) in each May over 02/201-06/2018 in zone 3.

**Fig. 4.** Trends with the uncertainty bars (STDs) of monthly mode reflectances 1) with no BRDF corrections (in black), 2) after the BRDF correction in this study (VIIRS BRDF-Cor-Ref; in red), and 3) after the Hu-BRDF correction based on MODIS band 1 (MODIS Hu-BRDF-Cor-Ref; in blue) normalized to their corresponding fitted values at the first data point in 02/2012 for M5 over 02/2012-06/2018 in the six aggregation zones Z1-Z6.

**Fig. 5.** Monthly mode reflectances 1) with no BRDF corrections (in black), 2) after the BRDF correction in this study (VIIRS BRDF-Cor-Ref; in red), and 3) after the Hu-BRDF correction based on MODIS band 1 (MODIS-Hu-BRDF-Cor-Ref; in blue) normalized to their corresponding fitted value at the first data point in 02/2012 for M5 during 02/2012 and 06/2018 in zone 3. The solid lines are the normalized linearly fitted reflectances.

**Fig. 6.** Trends (Left Panel) and STDs (Right Panel) of monthly mode reflectances before (in black) and after (in red) the BRDF correction normalized to their corresponding fitted values at the first data point in 02/2012 for M1-M5, M7-M11, and I1-I3. The dashed lines in trends represent the zero-trend lines and 2%-trend line for M9. The dashed lines in STDs represent the 2%-STD lines for the SWIR bands M9-M11 and I3.

**Fig. 7.** Numbers of monthly DCC samples in the six frame zones for M5 during February 2012 and May 2017. Z1: frames 1-640 for zone 1; Z2: frames 641-1008 for zone 2; Z3: frames 1009-1600 for zone 3; Z4: frames 1601-2192 for zone 4; Z5: frames 2193-2560 for zone 5; Z6: frames 2561-3200 for zone 6. The solid lines are the linearly fitted DCC sample numbers.

**Fig. 8.** Monthly BRDF-corrected mode reflectances normalized to their corresponding value at the first data point in 02/2012 in the six frame zones for the select RSB during February 2012 and June 2018. The solid lines are the normalized linearly fitted reflectances.

**Fig. 9.** Trends with the uncertainty bars (STDs) of monthly BRDF-corrected mode reflectances at 06/2018 along frames. The solid lines are the quadratic fitted trends against AOIs from DCC in black and from deserts in red for M1-M5, M7-M8, M10-M11, and I1-I3. The units are in percentage of fitted mode values in 02/2012.

**Fig. 10.** Reflectance from DCC before (DCC BRDF-Ref, in black) and after the correction by the DCC-derived RVS (DCC-RVS Corr BRDF-Ref, in red) against frame numbers over the six zones for M1-M5, M7-M8, M10-M11, and I1-I3. The units are in percentage of fitted reflectance values in 02/2012.

**Fig. 11.** Reflectance from deserts before (Desert BRDF-Ref, in black) and after the correction by the desert-derived RVS (Desert-RVS Corr BRDF-Ref, in red) against frame numbers over the 13 frames for M1-M5, M7-M8, M10-M11, and I1-I3. The units are in percentage of fitted reflectance values in 02/2012.

705 **Table 1** Center wavelengths (CW) of the eight Solar Diffuser Stability Monitor (SDSM)  
706 detectors in  $\mu\text{m}$ , and CW and bandwidths (BW) in nm and locations of the Focal Plane Assembly  
707 (FPA) of VIIRS RSB. Selected RSB in this study: 10 moderate resolution bands (M-bands, M1-  
708 M5 and M7-M11), and three imagery resolution bands (I-bands, I1-I3). M6 saturates over deep  
709 convective clouds (DCC).

710 **Table 2** Aggregation frame zones (Z1-Z6) for M-bands and aggregated I-bands at 750-m spatial  
711 resolution with 3200 frames along scan, and the frame number range, start scan angle, end scan  
712 angle, start zenith angle, end zenith angle, start AOI, and end AOI for each aggregation zone.

713 **Table 3** Trends and standard deviations (STDs) of monthly mode reflectances after the BRDF  
714 correction (BRDF-Cor-Ref) normalized to their corresponding fitted values at the first data point  
715 in 02/2012 for select RSB. Ranges represent for the spans of the trends and STDs among the Z1-  
716 Z6 for all bands. The units are in percentage of fitted mode values in 02/2012.

717 **Table 4** The corresponding desert site names (Sites) for the 13 desert frames (FR).